

Targeting cancer-associated fibroblast autophagy renders pancreatic cancer eradicable with immunochemotherapy by inhibiting adaptive immune resistance

Xiaozhen Zhang

Department of Hepatobiliary and Pancreatic Surgery, the First Affiliated Hospital, School of Medicine, Zhejiang University

Mengyi Lao

Department of Hepatobiliary and Pancreatic Surgery, the First Affiliated Hospital, School of Medicine, Zhejiang University

Hanshen Yang

Department of Hepatobiliary and Pancreatic Surgery, the First Affiliated Hospital, School of Medicine, Zhejiang University

Kang Sun

Department of Hepatobiliary and Pancreatic Surgery, the First Affiliated Hospital, School of Medicine, Zhejiang University

Lihong He

Department of Hepatobiliary and Pancreatic Surgery, the First Affiliated Hospital, School of Medicine, Zhejiang University

Muchun Li

Department of Hepatobiliary and Pancreatic Surgery, the First Affiliated Hospital, School of Medicine, Zhejiang University

Honggang Ying

Department of Hepatobiliary and Pancreatic Surgery, the First Affiliated Hospital, School of Medicine, Zhejiang University

Yan Chen

Xueli Bai

Department of Hepatobiliary and Pancreatic Surgery, the First Affiliated Hospital, School of Medicine, Zhejiang University

Tingbo Liang (✉ zhangshaw91@163.com)

Department of Hepatobiliary and Pancreatic Surgery, the First Affiliated Hospital, School of Medicine, Zhejiang University

Research Article

Keywords: Cancer-associated fibroblast, Autophagy, Adaptive immune resistance, PD-L1

Posted Date: November 9th, 2022

DOI: <https://doi.org/10.21203/rs.3.rs-2224090/v1>

License:  This work is licensed under a Creative Commons Attribution 4.0 International License.

[Read Full License](#)

Abstract

Background

Accumulating evidence suggests that cancer-associated fibroblast (CAF) autophagy is crucial in tumor development and may be a therapeutic target for pancreatic ductal adenocarcinoma (PDAC). However, the role of CAFs autophagy during immune surveillance and cancer immunotherapy is unclear.

Methods

In vivo efficacy and mechanistic studies, using ATG5f/f α -SMAcreERT2 mice, KPC-genetically engineered mouse model (GEMM) mice, C57BL/6 mice and nude mice with KPC cell-derived orthotopic tumors, employed immune checkpoint blockades (ICBs) and gemcitabine. Mass cytometry (CyTOF), immunohistochemistry (IHC), and flow cytometry analyzed local and systemic alterations in the immunophenotype. The regulatory effects of CAFs autophagy on tumour PD-L1 and its downstream signaling were analyzed by RNA-seq, 4D mass spectrometer (MS), IP-MS, western blotting, GST-pulldown, immunofluorescence (IF), IHC, and flow cytometry.

Results

The present study revealed that the inhibition of CAF autophagy suppresses *in vivo* tumor development in immune-deficient xenografts. This deletion compromises anti-tumor immunity and anti-tumor efficacy both *in vitro* and *in vivo* by upregulating PD-L1 levels in an immune-competent mouse model. A deletion in CAF autophagy reduced the production of interleukin 6, disrupting high desmoplastic TME and decreasing USP14 expression at the transcription level in pancreatic cancer cells. We further identify USP14 as the post-translational factor responsible for downregulating PD-L1 expression by removing K63 linked-ubiquitination at the K280 residue. Finally, chloroquine diphosphate-loaded mesenchymal stem cell (MSC)-liposome, by accurately targeting CAFs, inhibited CAF autophagy, improving the efficacy of immunochemotherapy to combat pancreatic cancer.

Conclusions

Targeting CAFs autophagy disrupt the desmoplastic and immunosuppressive TME to enhance the efficacy of immunochemotherapy by inhibiting adaptive immune resistance.

Introduction

Pancreatic ductal adenocarcinoma (PDAC) is notoriously resistant to chemotherapy, targeted therapies, and even immunotherapy, primarily due to abundant desmoplasia and an immunosuppressive tumor microenvironment (TME) (1-3). Thus, there is an urgent need to identify new treatments to remodel the TME that can improve the prognosis of this disease.

Multiple clinical trials of ICB therapy have been launched as a treatment for melanoma, lung cancer, and kidney cancer, with promising clinical results. However, it is estimated that, on average, 25% of patients with solid tumours response to ICB therapy, due to the presence of adaptive immune resistance (AIR) (4-7). Based on the presence of PDL1 expression and tumor infiltrating lymphocytes (TILs) (primarily based on CD8+ T cells), the tumours could be divided into four types: PDL1-/TIL- (type I); PDL1+/TIL+ (type II); PDL1-/TIL+ (type III); and PDL1+/TIL-(type IV) (8). A poor response to anti-PD therapy was observed in solid tumor patients with tumor immune microenvironment (TIME) types I, III and IV. Due to abundant desmoplasia and the immunosuppressive TME of pancreatic cancer, most pancreatic cancers belong to type I and type IV. Thus, ICB therapy has demonstrated limited effectiveness in PDAC to date (9, 10). In theory, an attractive strategy is to convert TIME types (I, III and IV) into type II, making them susceptible to anti-PD therapy in pancreatic cancer.

Carcinoma-associated fibroblasts (CAFs) play a crucial role in promoting the desmoplastic and immunosuppressive TME and thus represent potential therapeutic targets for cancer (11, 12). However, it remains unknown what role CAF autophagy plays in immune surveillance and cancer immunotherapy.

Here, we report that in PDAC, CAF autophagy plays a more important role in immune regulation and immunotherapy than the autophagy of tumor cells themselves. In detail, genetic and chemical autophagy inhibition of CAFs convert TME type I and type IV into type II so it could make sense to enhance the efficacy of ICB and gemcitabine treatment in immune-competent mouse models.

Methods

Mouse models

1) KPC (LSL-K-RasLSLG12D/+; LSL-p53R172H/+; Pdx1-Cre) genetically engineered mouse model was a kind gift from Prof. Raghu Kalluri (MD Anderson Cancer Center, Houston, TX, USA).

2) PDAC orthotopic model. Six-week-old male C57BL/6 and nude mice were purchased from the model animal research center of Nanjing University and housed in specific-pathogen-free (SPF) grade at the animal center, the First Affiliated Hospital, School of Medicine, Zhejiang University. KPC cells in addition with CAFs at a density of 3×10^5 / 3×10^5 in 12.5 μ L of serum-free McCoy's 5A mixed with 12.5 μ L of Matrigel were injected into the pancreas in front of the right side of the spleen using a sterile insulin needle inserted into a small left side abdominal incision near the spleen. The follow-up treatment commenced when the tumors reached 150-200 mm³, as detected by *in vivo* imaging.

3) ATG5f/f α -SMACreER^{T2} mice were generated by crossbreeding C57BL/6J-Atg5^{em1(flox)Cya} (TOS190429JN1, Cyagen Biosciences), and C57BL/6JSmoc-Acta2^{em1(CreERT2-Wpre-polyA) Smoc} (NM-KI-200074, Shanghai Model Organisms Center). At 6 weeks of age, tamoxifen was administered via an intraperitoneal injection (using an ACUC approved injection procedure) once every 24 h for a total of 5 consecutive days. For the Cre characterization work, there was a 14-day waiting period between the final injection and necropsy/histological analysis or PDAC orthotopic implantation.

Human/mouse CAFs and human/mouse PDAC cells

Human CAFs was established in the Department of Hepatobiliary and Pancreatic Surgery, the First Affiliated Hospital, Zhejiang University School of Medicine from fresh surgically resected tissues of PDAC patients using an enzymatic digestion method. Mouse CAFs was established in the Animal Center, the First Affiliated Hospital, Zhejiang University School of Medicine from fresh PDAC tissues from a KPC genetically engineered mouse model using the outgrowth method. The isolated cells were confirmed as CAFs as previously reported (13). Cell lines were maintained in Stellate Cell Medium (Sciencell 5301) supplemented with 10% fetal bovine serum (FBS), 1% Pen/ Strep (Cienry CR-15140) at 37°C in a humidified atmosphere containing 10% CO₂.

Mesenchymal stem cells (MSCs) isolated from a human umbilical cord were purchased from SinoCell Technology Ltd. (Ningbo, China). The MSCs were cultured in alpha-Minimal Essential Medium (alpha-MEM, VivaCell, China) supplemented with 10% non-heat inactivated fetal bovine serum, 10 ng/mL recombinant human epidermal growth factor (EGF) (PeproTech, USA), and 10 ng/mL human basic fibroblast growth factor (bFGF) (PeproTech, USA).

All PDAC cells, except KPCs, were purchased from the ATCC (American Type Culture Collection). These cells were grown in high-glucose Dulbecco's modified Eagle's medium (DMEM) (Gibco, Grand Island, NY, USA) supplemented with 10% FBS and 1% Pen/Strep (Cienry CR-15140). The KPC cell line, which was derived from tumor of an KPC genetically engineered mouse model, was cultured in modified McCoy's 5A Medium (Procell, China) containing 10% FBS and 1% Pen/Strep. All cell lines were routinely tested or mycoplasma contamination using PCR and found to be negative.

Flow cytometric analysis

For surface and intracellular PD-L1 and MHC-I staining of human and mouse cell lines, the cells were stained with PE/APC-anti-Human/Mouse CD274 antibodies after blocking using a TruStain FcX™ (BioLegend, anti-mouse CD16/32) antibody or Human TruStain FcX (BioLegend) at a 1:200 dilution for 30 min at 4°C in the dark and washed with FACS buffer (PBS plus 2% FBS and 2 mM EDTA). For cell-surface MHC-1 staining of human and mouse cells, single-cell suspensions and staining were prepared as described above. Dead cells were depleted by 7-AAD (BD biosciences) staining.

For tumour immunophenotyping, the tumor sample tissues were finely sliced into small fragments using scissors and scalpels, and incubated in DMEM containing 2% FBS + collagenase IV (1 mg/mL) (17104019, Thermo Fisher Scientific) +Dispase (0.6 mg/mL) (17105041, Gibco) + CaCl₂ (3 mM) (21115, Sigma-Aldrich) +DNase (10 µg/mL) (D5025, Sigma-Aldrich) under shaking at 200 - 220 rpm, 37°C for 20 - 40 mins. Dissociated tissues were filtered through 70 µm cell strainers (431751, BD Biosciences) and washed in DMEM without FBS and Pen/Strep after stopping the digestion by adding DMEM containing 10% FBS. The resuspended single cells were divided into two parts. Four-fifths of the cells were subjected to density gradient centrifugation to remove non-immune cells, and placed in 36% Percoll solution (17-0891-01, GE Healthcare) containing 4% 10XPBS and 60% serum free DMEM and. The isolated immune

cells were incubated with a Leukocyte Activation Cocktail (550583, BD biosciences) at 37°C for 4 - 6 h according to the manufacturer's instructions before being stained using a Fixable Viability Stain 780 (565388, BD biosciences) or LIVE/DEAD Fixable Violet Dead Cell Staining Kit (L34955, ThermoFisher Scientific) at 4°C for 20 – 30 min in the dark. Next, the cells were washed with FACS buffer, blocked using TruStain FcX™ (101320, BioLegend) antibody and stained for cell surface markers (CD45, CD3, CD4, CD8, and CD25) at 4°C for 30-40 min in the dark in FACS buffer. In addition, the cells were stained for intracellular cytotoxic CD8+T cell markers (Granzyme B and Perforin) in permeabilization solution after cells were subjected to fixation and permeabilization using a Fixation/Permeabilization Solution Kit (555028, BD biosciences). For one fifth of the tumor cells, cells were stained for PD-L1 and MHC-1 in the tumor cells (CD326+CD45-cells) at 4°C for 30 min in the dark after the cells were separated by live/dead cells and blocked.

To confirm immune cell depletion, the mouse spleens were mechanically ground with a grinding rod and filtered through a 40-µm cell strainers. The resuspended live single cells were stained separately using a LIVE/DEAD Fixable Violet Dead Cell Staining Kit and blocked using TruStain FcX™ after the red blood cells were removed using 1x lysis buffer (555899, BD biosciences). Finally, cells were stained for CD8+T cell markers (CD45, CD3 and CD8), and NK cells markers (CD49b and NK1.1). All samples were analyzed by BD LSRFortessa (BD biosciences) and the data were further analyzed by FlowJo software (Becton Dickinson).

***In vitro* deubiquitination assays**

HEK293T cells were co-transfected with K48- or K63-specific linkage His-ubiquitin plasmids and Flag-tagged PD-L1 plasmids. After a 48-h transfection, immunoprecipitation was performed to obtain ubiquitinated PD-L1, which was enriched using anti-Flag antibodies with agarose beads after treatment with MG132 (50 µM). The beads were washed three times using deubiquitinating buffer (4% glycerol, 5 mM MgCl₂, 60 mM HEPES, pH 7.6) and incubated with recombinant His-USP14 proteins at 37°C for 3 - 6 h. The mixtures were heated at 100°C for 5 min in 1 x SDS loading buffer and analyzed by an immunoblot analysis.

Duolink proximity ligation assay (PLA)

A Duolink proximity ligation assay between USP14 and PD-L1 performed by Duolink In Situ PLA kit (DUO92101, Sigma-Aldrich) according to the manufacturer's instructions. Briefly, cultured cells were fixed in 4% paraformaldehyde for 30 min at RT and permeabilized with 0.1% Triton X-100 for 15 min. Subsequently, the cells were blocked using a 1× blocking solution for 1 h at 37°C. The cells were then incubated with a USP14 and PD-L1 antibody in 1x antibody dilution buffer at 4°C overnight, followed by an incubation with PLA probes at 37°C for 1 h. After washing three times, the ligation-ligase solution was added and incubated at 37°C for 30 min. Next, the slides were incubated with an amplification-polymerase solution at 37°C in the dark for 100 min. Finally, the cells were stained with Mounting Medium containing DAPI. Fluorescent images were obtained with a Leica TCS SP8 and analyzed using LAS X software.

Endoplasmic reticulum enrichment and cell fractionation

Endoplasmic reticulum enrichment of pancreatic cancer cells was performed using an ER enrichment kit (Novus Biologicals) according to the manufacturer's instructions. The cytoplasmic fraction and nuclear fraction of pancreatic cancer cells was performed using the Cell Fractionation Kit (Cell Signaling Technology) in accordance with the manufacturer's instructions. All cell fractions were boiled with 1× SDS loading buffer and analyzed by immunoblotting.

Statistics

Molecular biology and biochemical experiments in vitro were routinely repeated at least three times. To compare the differences between the two groups, we used Mann-Whitney U or two-sided Student's t-tests as appropriate. We used a Spearman's rank correlation to analyze the correlation between variables. The overall difference in the data at the endpoint was assessed using Student's t-tests to evaluate the tumor growth. The Kaplan-Meier method and Gehan-Breslow-Wilcoxon test were used to detect difference in survival curves between groups. The GraphPad Prism software program (GraphPad Inc., La Jolla, CA, USA; version 7.0) was used to perform the statistical analyses. Results are presented as mean ± SD. Differences of $*P < 0.05$; $**p < 0.01$; $***P = 0.001$; and $****P < 0.001$ were considered statistically significant.

Results

Mutual regulation of CAF autophagy and activation in pancreatic cancer correlates with desmoplasia, an immunosuppressive TME, and poor patient survival.

Consistent with previous studies (13), IHC and IF revealed activated autophagy in CAFs in pancreatic cancer (Figure S1A, S1B and Figure 1A). By classifying our cohorts into autophagy-high and autophagy-low groups based on their IHC intensity and area, we found that autophagy in the cancer cells of patients was correlated with poor survival. It was also uncovered that autophagy in the patient's CAFs was correlated with poor survival (Figure 1B and C). To determine whether CAFs autophagy is relevant to AIR, we next evaluated collagen deposition and tumor-infiltrating immune cell populations in human PDAC tissues. Impressively, autophagy in CAFs, but not in cancer cells, were significantly correlated with increased collagen deposition and with fewer infiltrating CD8+ T cells (Figure 1D-G). Thus, the results indicated that autophagy in CAFs, but not in tumor cells correlated well with the induction of AIR in pancreatic cancer.

To determine the relationship between CAFs autophagy and activation, the correlation between LC3B and α -SMA was first identified in multiple assays, including, but not limited to transcription in the TCGA database and tumor tissue microarrays (Figure S1C-S1F). Furthermore, the transmission electron microscopy (TEM), immunofluorescence staining and immunoblotting results demonstrated that there was a significant reduction in the number of autophagosomes and inhibition of autophagic flux in CAFs treated with all-trans-retinoic acid (ATRA) to decrease CAFs activation (Figure 1H-L). In addition, the

inhibition of genetic (ATG5 knockdown) and chemical autophagy (Chloroquine) can promote CAFs to enter a quiescent state by the immunofluorescence staining and immunoblotting analyses (Figure 1M-P). The above results suggest that CAFs autophagy and activation in pancreatic cancer regulate each other, and correlate with AIR induction and poor patient survival.

Genetic inhibition of CAF autophagy induces PD-L1-upregulation, immune escape, and desmoplastic disruption in both immune-competent mice and pancreatic cancer cells

To investigate the effect of CAF autophagy on tumor cells *in vivo*, we orthotopically transplanted KPC with mouse CAFs(mCAFs)-WT or mCAFs-ATG5 KD cells into immunocompetent and immunodeficient mice (Figure 2A). The results in immunodeficient mice demonstrated that suppressing autophagy in mCAFs attenuated the effect of mCAFs on tumor growth and prolonged overall survival (OS) (Figure 2B-D), as previously reported (13). Intuitively, based on the results in immune-deficient mice and previous studies in our group (14, 15), it is expected that mCAFs-ATG5 KD tumors can significantly decrease the tumor size and improve OS in immunocompetent C57BL/6 mice compared to immunodeficient nude mice; however, no significant differences were observed between the mCAFs-ATG5 KD groups and mCAFs-WT group regarding tumor growth and survival in immunocompetent mice (Figure 2E-G). Moreover, we observed that the activity (GZMB+) of infiltrating CD8+ T cells was significantly decreased, whereas no difference was observed in the number of CD8+ T cells in the mCAFs-ATG5 groups by flow cytometry and immunohistochemistry (Figure 2H, I, Figure S2A and S2B). Unexpectedly, we observed an obvious upregulation in the level of PD-L1 protein expression in the tumor cells in the mCAFs-ATG5 KD group, which was associated with a significant decrease in the tumor-infiltrated GZMB+CD8+ T cell population (Figure 2H-M, Figure S2A and Figure S2B). To confirm this conclusion, we performed immunofluorescence, immunoblotting analysis, and flow cytometry in pancreatic cancer cell lines cocultured with CAFs-WT or CAFs-ATG5 KD to detect the level of PD-L1 expression. Similarly, these results were confirmed *in vitro* (Figure 2Q-P and Figure S3A-S3E). Functionally, we demonstrated that KPC cells cocultured with CAFs-ATG5 KD rendered the cells more resistant to activated CD8+ T cells in T cell-mediated tumor cell-killing assays (Figure 2S and 2T), which was similar to the *in vivo* results. Surprisingly, we found that MHC-1 expression was unchanged in tumor cells with CAFs-ATG5 KD by flow cytometry and immunoblotting analysis both *in vivo* and *in vitro* (Figure 2H, 2I, 2N, S3F and S3G). Similarly, no differences were found between the ctrl and chloroquine diphosphate (CQ)-treated groups in immunocompetent mice, compared to immunodeficient mice. In addition, tumours with a large number of CAFs are more resistant to CQ therapy than those with little or no CAFs (Figure S4). Collectively, these findings suggest that the inhibited CAF autophagy induces PD-L1 expression in tumour cells, which promotes pancreatic cancer cell immune escape both *in vitro* and *in vivo*.

Next, to examine the effect of genetic inhibition of CAF autophagy on disruption of high desmoplastic TME, IHC was performed to assess collagen deposition, CAF activation, and the microvascular area of the tumor tissues of immunocompetent C57BL/6 mice. The results demonstrated that the collagen area and α -SMA+CAF was sharply reduced, which indirectly promote tumour microvascular formation in KPC with the CAF ATG5 KD group (Figure S2A and S2B). Overall, these data indicate that the genetic inhibition of

CAF autophagy induced PD-L1 upregulation and disrupted desmoplasia in the PDAC mouse model. These changes function to convert TME type I (PDL1⁻/TIL⁻) into type II (PDL1⁺/TIL⁺), which may represent a prerequisite for enhancing the efficacy of ICB treatment for PDAC.

Inhibition of CAF autophagy improved the *in vivo* anti-tumor effect of immunotherapy.

Given that the inhibition of CAF autophagy can convert TME type I (PDL1⁻/TIL⁻) into type II (PDL1⁺/TIL⁺) in pancreatic cancer, one critical question is whether targeting CAF autophagy will have an effect on the therapeutic response to ICB treatment. Thus, we constructed a genetic mouse model ATG5f/f α -SMAcreER^{T2} mice to knockout ATG5 in the CAFs of PDAC *in vivo* to investigate the effect of inhibiting CAF autophagy on enhancing the efficacy of ICB treatment of PDAC (Figure 3A). As expected, the genetic deletion of CAF autophagy can enhance the therapeutic efficacy of PD-1-targeted drugs (Figure 3B-F). These tumours in ATG5f/f α -SMAcreER^{T2} combination with α PD-1 displayed increased infiltration and cytotoxic effects with bulk CD8 T cells and decreased number of Tregs (Figure 3G, 3H and Figure S5). In addition, the upregulation of PD-L1 expression in tumor cells was confirmed in ATG5f/f α -SMAcreER^{T2} mouse model by flow cytometry and CyTOF (Figure 3I and J; Figure S6). In particular, we found that the immune escape induced by inhibiting CAFs autophagy in immune-competent mice was substantially abrogated in *Cd274* knockout KPC mice. This finding confirms that the immune escape induced by inhibiting CAF autophagy is primarily dependent on the PD-1/PD-L1 signalling pathway (Figure S7A and S7B). At the endpoint, the efficiency of PD-L1 depletion using tumor cells from the mice was confirmed by flow cytometry (Figure S7C). In addition, CD8⁺ T cells or NK cells were depleted prior to an inoculation with KPC tumor cells with CAFs, and combined antibody treatment to determine which immune cell types were important for the effects of combination therapy. The efficacy of α PD-1 treatment was substantially abrogated by the administration of α CD8 α in mice bearing KPC tumors, whereas α NK1.1 partially inhibited the antitumor response in the combined treatment, indicating that NK cells play a more limited role compared to CD8⁺ T cells (Figure 3K). Finally, the survival analysis also demonstrated that survival time was significantly prolonged in an ATG5f/f α -SMAcreER^{T2} combination with α PD-1 compared with that in the other groups (Figure 3L).

Similar to α PD-1 treatment for PDAC, we observed that α PD-L1 and α CTLA4 treatment in ATG5f/f α -SMAcreER^{T2} mice also significantly decreased the tumor weight and prolonged the survival time compared with the other groups (Figure S8 and S9). To be closer to the clinical treatment, overt ATG5 f/f α -SMAcreER^{T2} mice bearing with tumors were treated with GEM or/and α PD-1. As expected, the ATG5 f/f α -SMAcreER^{T2} group were sensitized to GEM or GEM+ α PD-1 therapy, and exhibited drastically increased survival (Figure S10A-S10G). We further analyzed the response rate through three independently repeated treatment experiments in an orthotopic mouse model using an IVIS imaging system. The results showed that the response rate of the ATG5 f/f α -SMAcreER^{T2} with the GEM+ α PD-1 treatment group was significantly higher compared with that of the control and WT with GEM+ α PD-1 groups (Figure S10H).

Taken together, these results suggest that combining the inhibition of CAF autophagy and ICB may provide an effective treatment strategy to enhance the therapeutic efficacy of pancreatic cancer.

Deletion of CAF autophagy decreased the secretion of IL-6, which further increased PD-L1 expression via the ubiquitin proteasome system in pancreatic tumor cells.

To investigate the detailed mechanism of inhibited CAF autophagy induced PD-L1-upregulation immune escape, we determined the difference in cytokine expression between CAFs WT and CAFs ATG5 KD using a cytokine antibody array. The levels of IL-6, IL-11, M-CSF, RANTES, and sTNFR_{II} expression were significantly decreased in CAFs after ATG5 KD (Figure 4A and 4B). Furthermore, reduced levels of IL-6 derived from ATG5 KD CAFs were confirmed by ELISA (Figure 4C). In addition, the abundance of IL-6 expression in CAFs from pancreatic cancer tissue was significantly higher than other four cytokines in patient PDAC tissues and GEMM-KPC tumour tissues (Figure S11).

Next, to explore whether reduced IL-6 from ATG5 KD CAFs induced tumour PD-L1 expression, PD-L1 expression was examined in tumor cells with or without Tocilizumab treatment (IL-6R blockade) in CAFs-conditioned medium (CM) by flow cytometry, immunofluorescence, and immunoblotting analysis. The results demonstrated that the presence of increasingly elevated PD-L1 expression in tumour cells under CAFs-CM treated with Tocilizumab (Figure 4D-4H). Similar to previous reports, IL-6 upregulates PD-L1 expression by enhancing its association with N-glycosyltransferase STT3A in hepatocellular carcinoma (16). Thus, pancreatic cancer cells were treated with IL-6 to detect the level of PD-L1 expression by flow cytometry and immunoblotting analysis. Interestingly, decreased PD-L1 expression treated with IL-6 in SW1990 and Panc02 (PD-L1-high cell lines), while increased PD-L1 expression treated with IL-6 in PANC-1 and KPC (PD-L1-low cell lines), were detected by immunoblotting analysis (Figure S12A and S12B). By contrast, membrane PD-L1 expression remained unchanged under IL-6-treatment (Figure S12C). In addition, HLA-ABC/MHC-1 was not significantly affected by IL-6-treatment (Figure S12A). Indeed, CAFs-CM plus α IL-6R significantly attenuated the T cell-mediated cytotoxic effect in vitro compared with CAFs-CM (Figure 4I and 4J).

To determine how the IL-6 pathway blockade regulates the level of PD-L1 expression, the level of PDL1 mRNA remained unchanged in the tumor cells under CAFs treated with ATG5 KD-CM or Tocilizumab or α IL-6R (Figure 4K and 4L). Moreover, treatment with Tocilizumab or mouse α IL-6R induced PD-L1 protein expression, whereas the addition of the proteasome inhibitor, MG132, not the lysosome inhibitor, CQ, blocked PD-L1 protein degradation (Figure 4M), indicating that the IL-6 pathway blockade regulates PD-L1 expression via the ubiquitin proteasome system at the post-translational level. Indeed, PD-L1 in tumor cells under CAF-CM combined with Tocilizumab or α IL-6R treatment exhibited a longer half-life than the control groups, as well as lower levels of ubiquitination (Figure 4N-4P). In addition, we performed GeneOntology (GO) and enrichment plot of RNAseq in BxPC-3 with or without Tocilizumab treatment cocultured with CAFs for 24 h. The GO analysis showed that proteasomal protein catabolic process and ubiquitin protein ligase binding were significantly altered under Tocilizumab treatment (Figure S13A and Figure S13B).

Based on the above observations, our results indicate that the genetic inhibition of CAF autophagy decreased the level of IL-6 secretion, which further increased the level of PD-L1 expression by the ubiquitin proteasome system in pancreatic tumor cells.

Transcriptional activation of USP14 by STAT3 interacted with and negatively regulated PD-L1 in pancreatic cancer.

To further illustrate the underlying mechanism by which a IL-6 pathway blockade mediates PD-L1 regulation, we first performed an intersection analysis of the proteasome-mediated degradation pathway using RNAseq in BxPC-3 cells treated with or without Tocilizumab (50 ng/mL) and cocultured with CAFs and CD274 flag-IP-LCMS. 35 genes/proteins were shown in the intersection analysis (Figure 5A-C). We also identified deubiquitinating enzyme 14 (USP14) to represent a critical regulator of IL-6 pathway blockade-mediated PD-L1 regulation by an immunoblotting analysis (Figure 5D and Figure S13C). Bioinformatic analyses across multiple cancers demonstrated that USP14 was significantly upregulated in PAAD tissues compared with the level of expression in normal tissues (Figure S14). Such reduction in USP14 was also demonstrated in tumor cells under CAF ATG5 KD-CM (Figure 5E).

It has been well-established that STAT3 represents the most important downstream transcription factor of IL-6. Accordingly, we performed a CHIP assay to analyze the level of STAT3-bound potential binding site in the USP14 promotor. As shown in Figure 5F and G, one putative binding region in STAT3 was found and promoter constructs containing mutations in this region were generated to cause a STAT3-binding deficiency. To determine whether this STAT3 site was a transcriptionally active region, a dual luciferase assay was performed in 293T cell lines to test the expression of USP14 containing WT or MUT promoter elements for STAT3. STAT3-Flag cells exhibited a significantly higher level of USP14 expression compared to the negative CTRL in both SW1990 and PANC-1. Moreover, mutating the USP14 promoter reduced the expression in NC and STAT3-Flag cells. Similar results were observed after Tocilizumab treatment. Tocilizumab-treated cells had significantly lower USP14 expression than the CTRL group in SW1990 and PANC-1 cells. Mutating the USP14 promoter reduced the expression in the ctrl and Tocilizumab-treated cells (Figure 5H).

Furthermore, the results of the IP showed an endogenous interaction between USP14 and PD-L1 in multiple pancreatic cell lines (Figure 5I). Moreover, a glutathione S-transferase (GST)-pull down assay showed that USP14 bound to PD-L1 directly (Figure 5J). A Duo-link assay consistently demonstrated the binding between USP14 and PD-L1 in the cells (Figure 5K and L). USP14 inhibition (IU1) (deubiquitylating enzyme activity of USP14 was determined by HA-Ub-VS) or depletion increased the level of PD-L1 expression in pancreatic cancer by immunoblotting analysis, flow cytometry, and immunofluorescence (Figure 5M-T and Figure S15A-S15C). Functionally, a USP14 knockdown in pancreatic cancer cells *in vitro* increased the resistance of tumor cells to activated CD8⁺T cells in a T cell-mediated tumor cell-killing assay (Figure S15D and S15E). Next, we inoculated USP14 KD KPC cells into immunodeficient mice to study the effects *in vivo*. The tumor volume was significantly reduced in USP14 KD group compared with the WT group. In addition, a prolonged survival time was observed in the USP14 KD groups compared

with the WT group in immunodeficient mice; however, no significant differences were observed between the USP14 KD groups and the CTRL group in terms of tumor growth and survival in immunocompetent mice (Figure S16). To explore whether a USP14 deficiency enhanced the effect of αPD-1 therapy, αPD-1 was combined with IU1 in an immune-competent orthotopic model. Importantly, a combination with αPD-1 and IU1 further decreased the tumor weight and prolonged the animal survival time compared with that of other groups (Figure S17). Together, our results suggest that the transcriptional activation of USP14 by STAT3 interacted with and negatively regulated PD-L1 in pancreatic cancer.

USP14 destabilizes PD-L1 through specifically removing K63-linked poly-ubiquitination of PD-L1 at the K280 residue.

In contrast to upregulated PD-L1 expression following the USP14 deletion, USP14 overexpression decreased the level of PD-L1 expression in pancreatic cancer, which was accumulated by treatment with the proteasome inhibitor, MG132, suggesting that USP14 regulated PD-L1 expression via the proteasome system (Figure 6A and B). Indeed, the USP14 deletion exhibited a longer half-life than the control groups, and elevated K63-linked ubiquitination of PD-L1, which was reduced by K48-linked ubiquitination (Figure 6C-E). Moreover, an *in vitro* deubiquitination assay in a cell-free system further confirmed that USP14 could directly remove K63-linked ubiquitin chains from PD-L1, but not cleave the canonical K48-linked ubiquitination of PD-L1, since this would be expected to negatively regulate the abundance of PD-L1 protein expression (Figure 6F). Data from the Duolink assay indicated that the binding between PD-L1 and USP14 (Duo: red) occurred in the ER (Calnexin; green). The number of PD-L1-USP14 PLA dots were positively correlated with the level of calnexin fluorescence intensity (Figure 6H). In addition, the cell fractionation results showed that Eer I treatment indeed rescued the level of PD-L1 in the ER (Figure 6I).

PD-L1 is a transmembrane protein, and the cytoplasmic domain of PD-L1 (PD-L1-ICD; 260-290 residues) is involved in multiple regulation pathways controlling PD-L1 protein ubiquitination and degradation (17). Therefore, we speculated that USP14 can remove ubiquitin chains from the ICD region of PD-L1. Two evolutionarily conserved USP14 ubiquitination-specific motifs were identified across multiple species, centering at the K271 and K280 residues, were further confirmed by a ubiquitinationomic analysis (Figure 6J and K). We constructed GFP-PD-L1 K271R and GFP-PD-L1 K280R mutants to examine whether USP14 could affect GFP-PD-L1 K271/280R expression and ubiquitination. In PD-L1 KO KPC cells, the K280R mutant displayed significantly decreased levels of PD-L1 expression, compared with GFP-WT PD-L1 and GFP-K271R PD-L1 (Figure 6L). Furthermore, in USP14 KD KPC cells, the ubiquitination of GFP-WT PD-L1 was significantly increased, whereas the K280R mutant displayed virtually no ubiquitination (Figure 6M). Thus, USP14 destabilizes PD-L1 through specifically removing K63-linked poly-ubiquitination of PD-L1 at the K280 residue, but not K271, as confirmed by a bioinformatics analysis (Figure S18).

Targeting CAF autophagy renders primary PDAC tumors eradicable by immunotherapy via engineering stem cell-derived biomimetic vesicles

To explore the efficacy of combination therapy between ICB and the inhibition of autophagy in PDAC, we found that inhibiting chemical autophagy (chloroquine) sensitizes PDAC tumours to ICB therapy (Figure

S19), as previous reports(18). However, inhibition autophagy by chloroquine via an intraperitoneal administration orthotopic mouse model could not specifically target CAFs autophagy. Thus, to achieve targeted delivery of chloroquine diphosphate (CQ) to CAFs, a biomimetic drug delivery system, termed mesenchymal stem cell (MSC)-Lipo, was prepared according to the procedure illustrated in Figure 7A, as previously reported (19, 20).

The hydrodynamic size of MSC-Lipo was $74.267 \text{ nm} \pm 14.614 \text{ nm}$ and the zeta potential of MSC-Lipo decreased to $-3.980 \text{ mV} \pm 0.314 \text{ mV}$ with the addition of negative charges of the MSC membrane (Figure S20A). The results of transmission electron microscopy (TEM) showed that MSC-Lipo exhibited a clear and complete bilayer structure with no adhesion (Figure 7B and Figure S20B). The colocalization of liposomes (labeled by DiD, red) and MSC membrane (labeled by DiO, green) illustrated that these two components were well integrated at a weight ratio of 1:0.5 (Figure S20C). The immunoblot analysis indicated that MSC-specific marker proteins (e.g., CD105, CD90, and CD44) were preserved after membrane integration using a sonication probe (Figure 7C). The total protein profile of MSC-Lipo was consistent with that of the MSC membrane, whereas liposomes did not exhibit any protein expression according to SDS-PAGE results (Figure 7D). The MSC-Lipo characterization results indicated that MSC-Lipo inherited some properties of specific proteins on the surface of the MSC was successfully prepared. Furthermore, MSC-Lipo also maintained $48.123\% \pm 0.696\%$ drug encapsulation efficiency of CQ after sonication (Figure 7E). Therefore, stable drug loading capability lays the foundation for MSC-Lipo as a drug delivery carrier.

To investigate the delivery capacity of MSC-Lipo in an orthotopic pancreatic TME, the cellular uptake and tumor targeting ability of MSC-Lipo were evaluated both *in vitro* and *in vivo*. The flow cytometry and IF analysis and demonstrated that MSC-Lipo has a better uptake in mCAFs than KPC cells (Figure 7F-7H). Compared with free-DiD, MSC-Lipo presented a stronger tumor targeted ability *in vivo* imaging system, especially 12 h after intravenous injection (Figure 7I-J). Moreover, to further study the cellular uptake in tumor tissues, the result demonstrated that a substantial amount of MSC-Lipo was taken up by the mCAFs (orange fluorescence) (Figure 7K). Both the *in vitro* and *in vivo* results confirmed that MSC-Lipo could targeting deliver drugs to mCAFs rather than KPC.

Furthermore, the anti-tumor effect of α PD-1 combined with CQ-loaded MSC-Lipo was explored in mice with orthotopic pancreatic cancer. The outcomes proved that α PD-1 combined with CQ-MSC-Lipo most effectively suppressed tumor growth, which was especially reflected in the tumor volume and weight. Surprisingly, compared with an intraperitoneal injection of free CQ, an intravenous injection of CQ-MSC-Lipo exerted a better anti-tumor effect with the reduction of the dosage to 4.6% and a dosing frequency of 33.33% at the same time (Figure 7L and M). There was no significant difference in body weight between each group at the end of treatment (Figure 7N), whereas all groups were within the normal range for liver and kidney function (Figure S21A). The weight to body ratio of each organ and H&E staining did not reveal a significant difference between each group (Figure S21B and S21C), indicating that CQ-MSC-Lipo had substantial biocompatibility in the treatment of pancreatic cancer.

In conclusion, the findings of our study revealed that a deletion in CAFs autophagy reduced the level of IL-6 production, disrupting desmoplasia, and decreasing the level of USP14 expression transcription in pancreatic cancer cells. Indeed, we identified USP14 as the post-translational factor upregulating PD-L1 expression by removing K63 linked-ubiquitination at the K280 residue. Functionally, the autophagy-deficient CAFs improve the efficacy of PD-1/PD-L1 mAbs and gemcitabine treatment of pancreatic cancer in an immune-competent mouse model (Figure 8).

Discussion

It has increasingly become the consensus that the TME comprises a heterogeneous population of CAFs with different functions rather than comprising a uniform population of cells within PDAC tumors. Based on the expression pattern of various fibroblast markers *in vivo*, the existence of distinct myofibroblastic CAFs (myCAFs) (α SMA^{high} IL-6^{low}), inflammatory CAFs (iCAFs) (α SMA^{high} IL-6^{low}) and antigen-presenting CAF (apCAF) (MHC class II+ CD74+) subpopulations were confirmed in a KPC mouse model and PDAC patient samples (21, 22). Both our study and previous reports have revealed that CAF autophagy is positively correlated with the activation of pancreatic cancer, and is associated with poor outcomes (shorter survival time and disease recurrence) for patients with pancreatic cancer (13). Interestingly, data from our study demonstrated that autophagy activation in CAFs (α SMA+) was accomplished by IL-6 secretion. Thus, in contrast to the above three subtypes, α SMA^{high} IL-6^{high} CAFs may exist independently, suggesting that autophagy may also be an important signature for characterizing different CAF subtypes.

The studies have reported that the inhibition of CAF autophagy markedly inhibited the tumor growth of pancreatic cancer and head and neck squamous cell carcinoma in nude mice (13, 23). In our study, this result was confirmed in nude mice; however, no significant differences were observed in tumor growth and survival following the inhibition of autophagy in CAFs in immunocompetent mice. Our results revealed that the mechanism through which this deletion induces PD-L1 upregulation, which inactivates cocultured T cells *in vitro*, compromises anti-tumor immunity *in vivo* and reduces anti-tumor efficacy in an immune-competent mouse model. Recently, we have explored in-depth how to improve the therapeutic efficacy of α PD-1/PD-L1 in both pancreatic and liver cancer (14, 15, 24). In these previous studies in our group, we have focused on improving the therapeutic efficacy of α PD-L1 in PDL1+/TIL+ (type II) or/and PDL1+/TIL-(type IV) tumors by targeting the crucial regulators of PD-L1 to reduce the level of PD-L1 protein expression. Although this makes up for the poor therapeutic efficacy caused by incomplete blocking of α PD-L1, TME type I (PDL1-/TIL-) and type III (PDL1-/TIL+), classified as “target-missing”, occur in 60% - 85% of solid tumours (7). Especially in pancreatic cancer, a lack of PD-L1 protein expression exists in most patient samples from our data. Since anti-PD therapy functions by blocking the interaction between PD1 and PDL1, a lack of expression of one or both proteins in the TME would not allow this therapy to function, in theory. Thus, a practical approach is to convert TME type I (PDL1-/TIL-) or type III (PDL1-/TIL+) into type II (PDL1+/TIL+), making them susceptible to anti-PD therapy. This strategy has also been confirmed by recently published studies (25, 26).

To explore the clinical utility of our results in the future, we searched for clinical trials investigating CQ-treated in pancreatic cancer. The results showed that the combination of gemcitabine hydrochloride and nab-paclitaxel (GA) with hydroxychloroquine sulfate (HCQ) did not improve the primary end point of OS at 12 months (27). In addition, two other clinical trials have not published any results (NCT02071537 and NCT01777477). According to the preclinical results in this paper, one reason for the negative results of the clinical trials is that the inhibition of autophagy induces the upregulation of PD-L1 expression to suppress anti-tumor efficacy. Therefore, based on chemotherapy and chloroquine, additional ICB immunotherapy can achieve a better clinical treatment effect and prolong the survival time of PDAC patients.

In summary, we uncover an interesting and innovative story about pancreatic cancer: CAFs activation strengthens the physical barrier by eating self, blocking the infiltration of anti-tumor drugs and immune cells, and makes the tumor highly level of ubiquitination to cause the “target-missing” of PD-L1 in pancreatic cancer, which further formed the immune desert of pancreatic cancer to avoid being killed by CD8+ T cells. In short, eating self of CAFs for not to be eaten of tumor cells. Thus, disrupting the “self-sacrifice” of CAFs paved the way for further clinical trials to evaluate their clinical impact on patients with PDAC.

Declarations

Author contributions

All authors meet authorship requirements. Conception and design were performed by XZ, XB, and TL. Development of methodology was taken part by XZ and ML. Acquisition of data (provided animals, acquired and managed patients, provided facilities, etc.) was performed by XZ, ML, HY, KS and ML. Analysis and interpretation of data (e.g., statistical analysis, biostatistics, computational analysis) were carried out by XZ and LH. Writing, review, and/or revision of the manuscript were performed by XZ, XB, and TL. Administrative, technical, or material support (i.e., reporting or organizing data, constructing databases) was taken part by XZ, HY, and YC. Study supervision was carried out by XB, and TL. All authors read and approved the final manuscript.

Funding

This work was supported by grants from the National Key Research and Development Program [2019YFC1316000 to TBL]; the National Natural Science Foundation of China [U20A20378, 82188102 and 81830089 to TBL, 81871925 and 82071867 to XLB].

Availability of data and materials

The datasets supporting the conclusions of this article are included within the article and its additional files.

Ethics approval and consent to participate

All animal work was approved by IACUC of the First Affiliated Hospital, School of Medicine, Zhejiang University. The human PDAC tumor samples used in this paper were collected from the Department of Hepatobiliary and Pancreatic Surgery, the First Affiliated Hospital, School of Medicine, Zhejiang University. The study protocol was approved by the Institutional Review Board of First Affiliated Hospital, School of Medicine, Zhejiang University. All tissue samples were collected in compliance with the informed consent policy.

Competing interests

The authors have declared that no conflicts of interest exist.

Consent for publication

All authors approved and directly participated in the planning, execution and/ or analysis of the data presented in this study. The content of this manuscript has not been previously published and is not under consideration for publication elsewhere.

References

1. Kleeff J, Korc M, Apte M, La Vecchia C, Johnson CD, Biankin AV, et al. Pancreatic cancer. *Nature Reviews Disease Primers*. 2016;2.
2. Ho WJ, Jaffee EM, Zheng L. The tumour microenvironment in pancreatic cancer – clinical challenges and opportunities. *Nature Reviews Clinical Oncology*. 2020;17(9):527-40.
3. Binnewies M, Roberts EW, Kersten K, Chan V, Fearon DF, Merad M, et al. Understanding the tumor immune microenvironment (TIME) for effective therapy. *Nature Medicine*. 2018;24(5):541-50.
4. Emens LA, Cruz C, Eder JP, Braiteh F, Chung C, Tolaney SM, et al. Long-term Clinical Outcomes and Biomarker Analyses of Atezolizumab Therapy for Patients With Metastatic Triple-Negative Breast Cancer: A Phase 1 Study. *JAMA Oncol*. 2019;5(1):74-82.
5. Garon EB, Rizvi NA, Hui R, Leighl N, Balmanoukian AS, Eder JP, et al. Pembrolizumab for the treatment of non-small-cell lung cancer. *N Engl J Med*. 2015;372(21):2018-28.
6. Zhu AX, Finn RS, Edeline J, Cattani S, Ogasawara S, Palmer D, et al. Pembrolizumab in patients with advanced hepatocellular carcinoma previously treated with sorafenib (KEYNOTE-224): a non-randomised, open-label phase 2 trial. *Lancet Oncol*. 2018;19(7):940-52.
7. Kim TK, Vandsemb EN, Herbst RS, Chen LP. Adaptive immune resistance at the tumour site: mechanisms and therapeutic opportunities. *Nature Reviews Drug Discovery*. 2022;21(7):529-40.
8. Zhang Y, Chen L. Classification of Advanced Human Cancers Based on Tumor Immunity in the MicroEnvironment (TIME) for Cancer Immunotherapy. *JAMA Oncol*. 2016;2(11):1403-4.
9. O'Reilly EM, Oh DY, Dhani N, Renouf DJ, Lee MA, Sun W, et al. Durvalumab With or Without Tremelimumab for Patients With Metastatic Pancreatic Ductal Adenocarcinoma: A Phase 2 Randomized Clinical Trial. *JAMA Oncol*. 2019;5(10):1431-8.

10. Brahmer JR, Tykodi SS, Chow LQ, Hwu WJ, Topalian SL, Hwu P, et al. Safety and activity of anti-PD-L1 antibody in patients with advanced cancer. *N Engl J Med*. 2012;366(26):2455-65.
11. Sahai E, Astsaturov I, Cukierman E, DeNardo DG, Egeblad M, Evans RM, et al. A framework for advancing our understanding of cancer-associated fibroblasts. *Nature Reviews Cancer*. 2020;20(3):174-86.
12. Whittle MC, Hingorani SR. Fibroblasts in Pancreatic Ductal Adenocarcinoma: Biological Mechanisms and Therapeutic Targets. *Gastroenterology*. 2019;156(7):2085-96.
13. Endo S, Nakata K, Ohuchida K, Takesue S, Nakayama H, Abe T, et al. Autophagy Is Required for Activation of Pancreatic Stellate Cells, Associated With Pancreatic Cancer Progression and Promotes Growth of Pancreatic Tumors in Mice. *Gastroenterology*. 2017;152(6):1492+.
14. Zhang X, Huang X, Xu J, Li E, Lao M, Tang T, et al. NEK2 inhibition triggers anti-pancreatic cancer immunity by targeting PD-L1. *Nat Commun*. 2021;12(1):4536.
15. Zhang X, Lao M, Xu J, Duan Y, Yang H, Li M, et al. Combination cancer immunotherapy targeting TNFR2 and PD-1/PD-L1 signaling reduces immunosuppressive effects in the microenvironment of pancreatic tumors. *J Immunother Cancer*. 2022;10(3).
16. Chan LC, Li CW, Xia W, Hsu JM, Lee HH, Cha JH, et al. IL-6/JAK1 pathway drives PD-L1 Y112 phosphorylation to promote cancer immune evasion. *J Clin Invest*. 2019;130.
17. Wen M, Cao Y, Wu B, Xiao T, Cao R, Wang Q, et al. PD-L1 degradation is regulated by electrostatic membrane association of its cytoplasmic domain. *Nat Commun*. 2021;12(1):5106.
18. Yamamoto K, Venida A, Yano J, Biancur DE, Kakiuchi M, Gupta S, et al. Autophagy promotes immune evasion of pancreatic cancer by degrading MHC-I. *Nature*. 2020;581(7806):100-5.
19. Wu H, Jiang X, Li Y, Zhou Y, Zhang T, Zhi P, et al. Engineering Stem Cell Derived Biomimetic Vesicles for Versatility and Effective Targeted Delivery. *Advanced Functional Materials*. 2020;30(49):2006169.
20. Li YS, Wu HH, Jiang XC, Zhang TY, Zhou Y, Huang LL, et al. Active stealth and self-positioning biomimetic vehicles achieved effective antitumor therapy. *J Control Release*. 2021;335:515-26.
21. Elyada E, Bolisetty M, Laise P, Flynn WF, Courtois ET, Burkhart RA, et al. Cross-Species Single-Cell Analysis of Pancreatic Ductal Adenocarcinoma Reveals Antigen-Presenting Cancer-Associated Fibroblasts. *Cancer Discov*. 2019;9(8):1102-23.
22. Öhlund D, Handly-Santana A, Biffi G, Elyada E, Almeida AS, Ponz-Sarvise M, et al. Distinct populations of inflammatory fibroblasts and myofibroblasts in pancreatic cancer. *J Exp Med*. 2017;214(3):579-96.
23. New J, Arnold L, Ananth M, Alvi S, Thornton M, Werner L, et al. Secretory Autophagy in Cancer-Associated Fibroblasts Promotes Head and Neck Cancer Progression and Offers a Novel Therapeutic Target. *Cancer Research*. 2017;77(23):6679-91.
24. Huang X, Zhang Q, Lou Y, Wang J, Zhao X, Wang L, et al. USP22 deubiquitinates CD274 to suppress anti-cancer immunity. *Cancer Immunol Res*. 2019.

25. Koikawa K, Kibe S, Suizu F, Sekino N, Kim N, Manz TD, et al. Targeting Pin1 renders pancreatic cancer eradicable by synergizing with immunochemotherapy. *Cell*. 2021;184(18):4753-71.e27.
26. Liu H, Kuang X, Zhang Y, Ye Y, Li J, Liang L, et al. ADORA1 Inhibition Promotes Tumor Immune Evasion by Regulating the ATF3-PD-L1 Axis. *Cancer Cell*. 2020;37(3):324-39.e8.
27. Karasic TB, O'Hara MH, Loaiza-Bonilla A, Reiss KA, Teitelbaum UR, Borazanci E, et al. Effect of Gemcitabine and nab-Paclitaxel With or Without Hydroxychloroquine on Patients With Advanced Pancreatic Cancer: A Phase 2 Randomized Clinical Trial. *JAMA Oncol*. 2019;5(7):993-8.

Figures

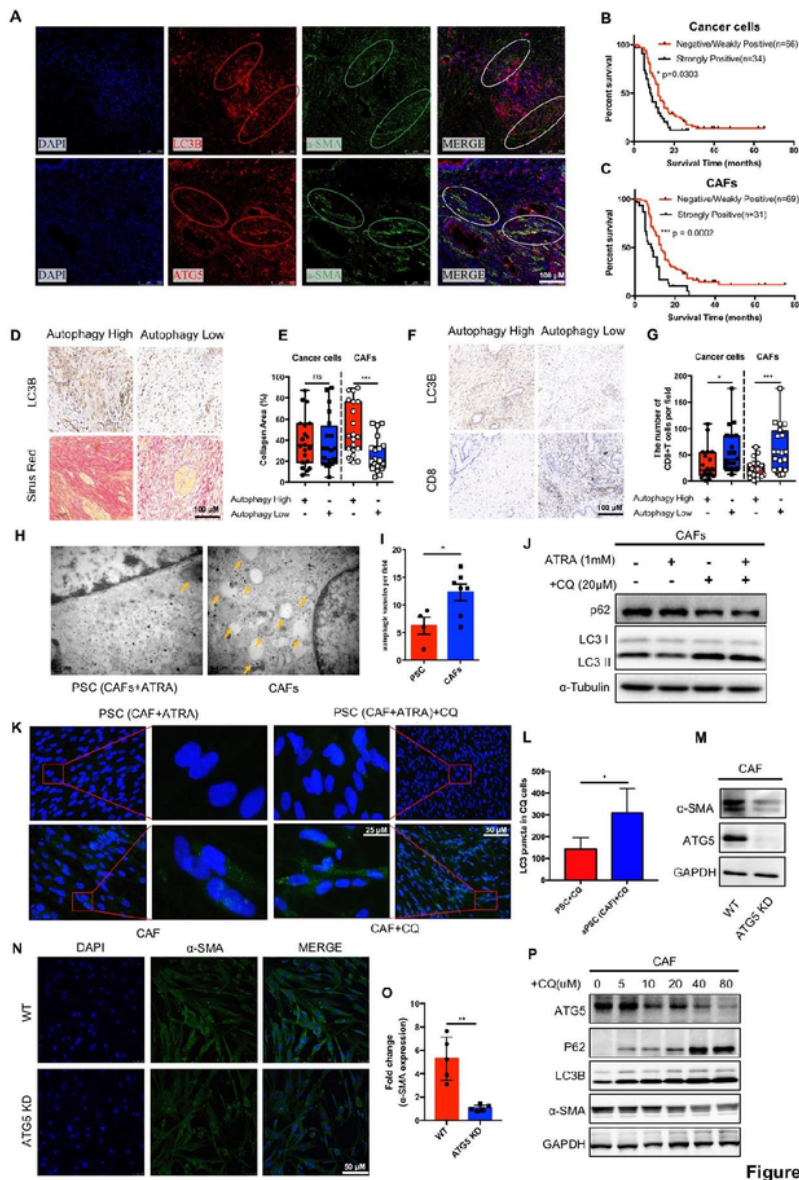


Figure 1

Figure 1

Mutual regulation of CAF autophagy and activation in pancreatic cancer.

(A) Immunofluorescence staining for LC3B, α-SMA, and DAPI in PDAC. A portion of α-SMA-expressing spindle cells exhibited LC3B staining (white arrowheads).

(B and C) Tissue microarray analysis of the prognostic role of LC3B expression in cancer cells and CAFs in pancreatic cancer.

(D and E) LC3B IHC and Sirius Red staining in human PDAC tissues and quantification of collagen deposition using Sirius Red staining.

(F and G) LC3B and CD8 IHC staining in human PDAC tissues, and quantification of the CD8 positive cell area per field.

(H and I) Representative transmission electron microscopy images and statistical results of autophagosomes and autolysosomes in CAFs after adding ATRA (1 mM) or PBS.

(J) Western blot analysis of LC3B and P62 in CAFs and iPSC (CAF treated after ATRA) with or without CQ.

(K and L) Representative microphotographs and statistical results of LC3B immunofluorescence staining in CAFs following CQ treatment. The addition of CQ to CAFs induced an accumulation of LC3 in the cytoplasm.

(M) CAFs were subjected to ATG5 KD, followed by IB for the different indicated proteins.

(N and O) CAFs were subjected to ATG5 KD, followed by IB for α -SMA (green) and DAPI (blue).

(P) CAFs were treated with CQ and then subjected to IB for the different indicated proteins.

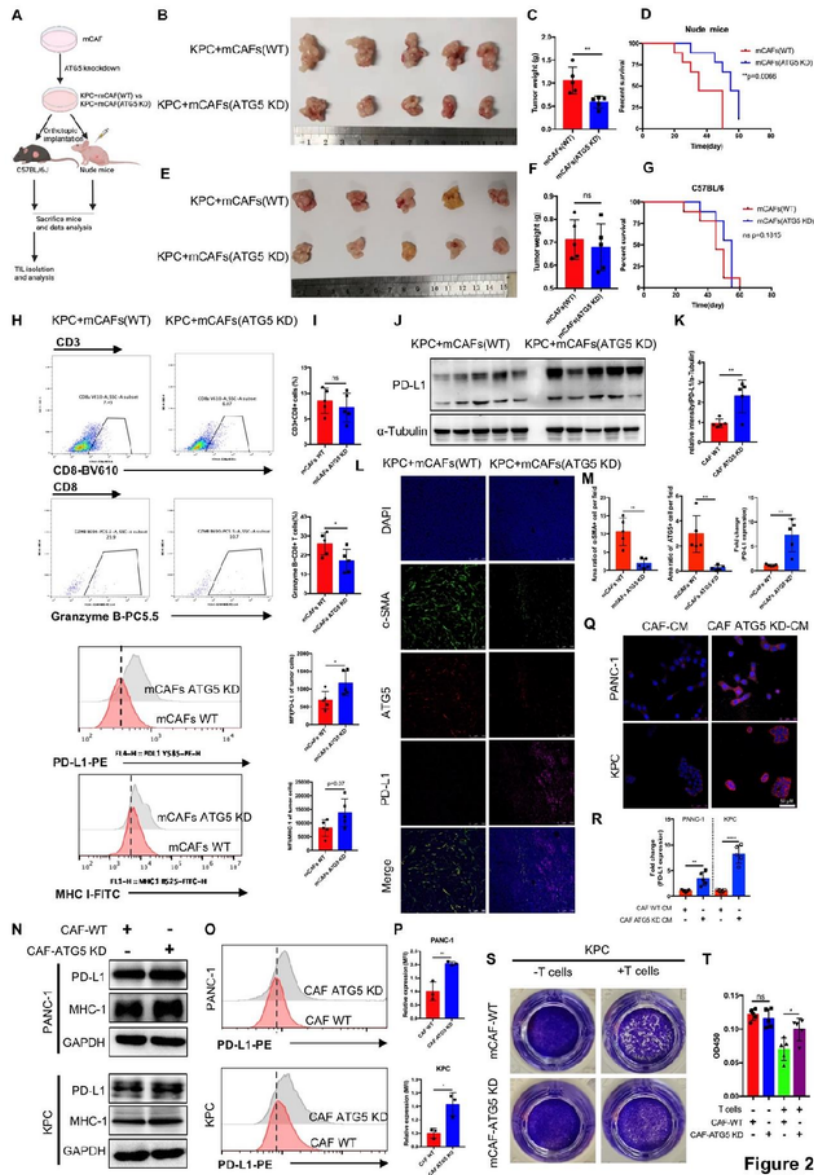


Figure 2

Figure 2

Genetic inhibition of CAF autophagy induced PD-L1-upregulation mediated immune escape in both immune-competent mice and pancreatic cancer cells.

(A) Schematic protocols of WT-mCAFs and ATG5 KD-mCAFs with KPC separately and s.c. injected into immunocompetent and immunodeficient mice (n = 5).

(B-G) Representative images displaying tumors, tumor weight, and survival of immunocompetent and immunodeficient mice bearing WT-mCAFs and ATG5 KD-mCAFs with KPC.

(H and I) Representative images and statistical results of tumor-infiltrating lymphocytes and immunomodulators in tumor cells (n = 5).

(J and K) Immunoblot analysis of PD-L1 expression in pancreatic tumors with ATG5 KD-mCAFs.

(L and M) Representative images and further quantification of tumor-bearing ATG5 KD-CAFs followed by immunofluorescence staining for α -SMA (green), ATG5 (red), PD-L1 (pink) and DAPI (blue).

(Q and R) Representative images and further quantification of tumor cells cocultured with ATG5 KD-CAFs followed by immunofluorescence staining for PD-L1 (red) and DAPI (blue).

(N) Immunoblot analysis of PD-L1 and MHC-1 expression in tumor cell lines cocultured with WT-CAFs and ATG5 KD-CAFs.

(O and P) Flow cytometry and further quantification of PD-L1 expression in tumor cell lines cocultured with WT-CAFs and ATG5 KD-CAFs.

(S and T) Representative images and statistical results of T cell-mediated cancer cell-killing assay. KPC cells were pre-cocultured with WT-CAFs and ATG5 KD-CAFs for 24 h, then cocultured with activated T cells for 48 h and subjected to crystal violet staining. The ratio of tumor cells to T cells was 1:8.

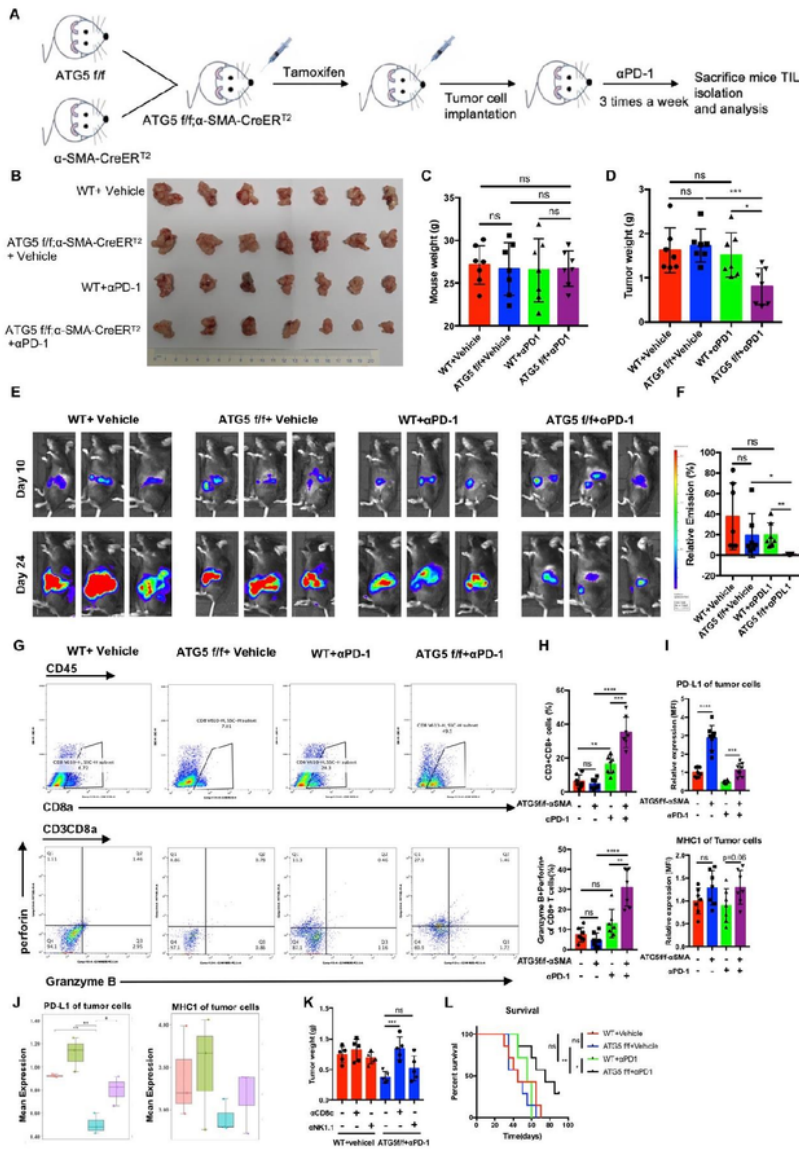


Figure 3

Figure 3

Inhibition of CAF autophagy improved the *in vivo* anti-tumor effect of immunotherapy.

(A) Schematic protocol for the genetic inhibition of CAF autophagy combined with anti-PD-1 antibodies.

(B-D) Representative images displaying tumors, tumor weight, and mouse weight of ATG5f/f- α SMAcreER^{T2} genetic mice treated with anti-PD-1 antibodies.

(E and F) Representative photograph and statistical results of the IVIS imaging system in mice orthotopically implanted with luciferase-expressing KPC in ATG5f/f- α SMAcreER^{T2} genetic mice.

(G-I) Flow cytometric analysis and statistical results of lymphocytes that have infiltrated the tumors and membrane PD-L1 and MHC-1 expression on tumor cells (n = 7).

(J) CyTOF analysis of membrane PD-L1 and MHC-1 expression on tumor cells in the four treatment groups (n = 3).

(K) The statistical results of tumor weight following pretreatment with anti-CD8 α and anti-NK1.1 in ATG5f/f- α SMAcreER^{T2} genetic mice combined with anti-PD-1 antibodies.

(L) Survival curve of orthotopic tumor implantation in ATG5f/f- α SMAcreER^{T2} genetic mice. ATG5f/f- α SMAcreER^{T2} genetic mice-orthotopic mice were treated with anti-PD-1 antibodies until the mice were at the point of death and met the prespecified early removal criteria approved by the IACUC

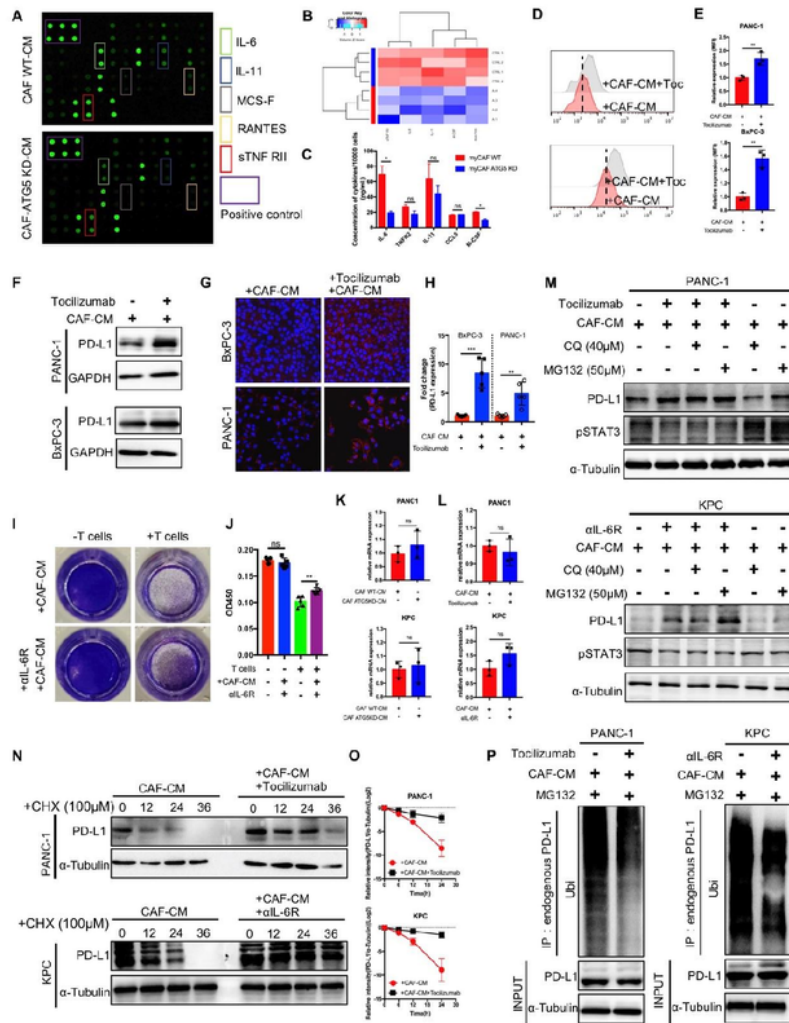


Figure 4

Figure 4

Deletion of CAF autophagy decreased IL-6 secretion, which further increased PD-L1 expression by the ubiquitin proteasome system in pancreatic tumor cells.

(A and B) Differential cytokine expression was detected between WT and ATG5 KD CAFs using a cytokine antibody array and further quantified with a heatmap analysis.

(C) The concentration of the top five secreted cytokines in the cytokine antibody array was identified by an ELISA.

(D and E) Flow cytometric analysis and statistical results of PD-L1 expression in tumor cells with or without Tocilizumab under CAF-conditioned medium.

(F) Immunoblot analysis of PD-L1 expression in tumor cells with or without Tocilizumab-treated CAFs.

(G and H) Representative images and further quantification of tumor cells with or without Tocilizumab-treated CAFs.

(I and J) Representative images and statistical results of the T cell-mediated cancer cell-killing assay. KPC cells with or without α L-6R pre-cocultured CAFs for 24 h were cocultured with activated T cells for 48 h and subjected to crystal violet staining. The ratio of tumor cells to T cells was 1:8.

(K) qRT-PCR examination of PD-L1 expression in tumor cells cocultured with WT-CAF and ATG5 KD-CAF for 24 h.

(L) qRT-PCR examination of PD-L1 expression in tumor cells with or without Tocilizumab treated CAFs.

(M) Immunoblot analysis of CAFs treated with Tocilizumab or α L-6R for 24 h with and without chloroquine (40 μ M for last 6 h of treatment) or MG132 (20 μ M for last 6 h of treatment).

(N and O) Stability analysis of PD-L1 in tumor cells treated with or without Tocilizumab or α L-6R cocultured with CAFs following treatment with cycloheximide (CHX).

(P) Ubiquitination assay of PD-L1 in tumor cells treated with or without Tocilizumab or α L-6R and cocultured with CAFs after treatment with MG132.

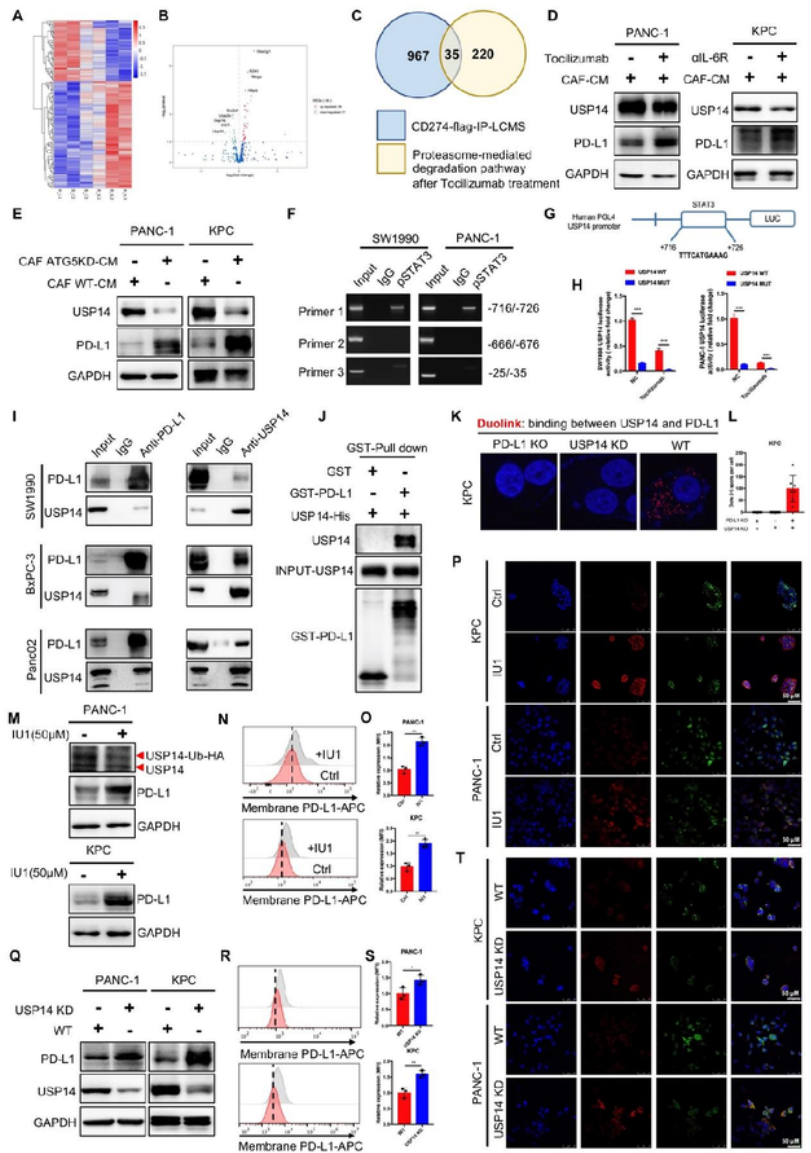


Figure 5

Figure 5

Transcriptional activation of USP14 by STAT3 interacted with and negatively regulated PD-L1 in pancreatic cancer.

(A and B) Heatmap and volcano plot of RNAseq in BxPC-3 with or without Tocilizumab treatment cocultured with CAFs for 24 h.

(C) Intersection analysis of the proteasome-mediated degradation pathway in RNAseq and CD274 flag-IP-LCMS.

(D) Immunoblot analysis of USP14 expression in tumor cells with or without Tocilizumab or aIL-6R treatment and cocultured with CAFs

(E) Immunoblot analysis of USP14 expression in tumor cells cocultured with WT-CAFs and ATG5 KD-CAFs for 48 h.

(F) Chromatin immunoprecipitation (ChIP) assay analysis of the STAT3-bound potential binding site in the USP14 promoter.

(G and H) Schematic representation of the USP14 promoter cloned into the pGL4 vector. The predicted STAT3-binding motifs were shown and the promoter constructs containing mutations in this region to cause a STAT3-binding deficiency were generated.

(I) Cell lysates from SW1990, BxPC-3, and Panc02 were separately analyzed by IP and Western blotting using the antibodies indicated. Representative images are shown.

(J) GST-pull down assay of USP14-His and GST-PD-L1 proteins. Representative images are shown.

(K and L) Representative images and statistical results of individual immunofluorescence staining of the USP14 and PD-L1 interaction in KPC cells by a Duolink assay. The red dots (USP14/PD-L1 interaction) indicate their interaction.

(M-T) Immunoblot analysis, flow cytometric analysis, and immunofluorescence staining of PD-L1 expression in tumor cells following treatment with IU1 (USP14 inhibitor) and USP14 knockdown.

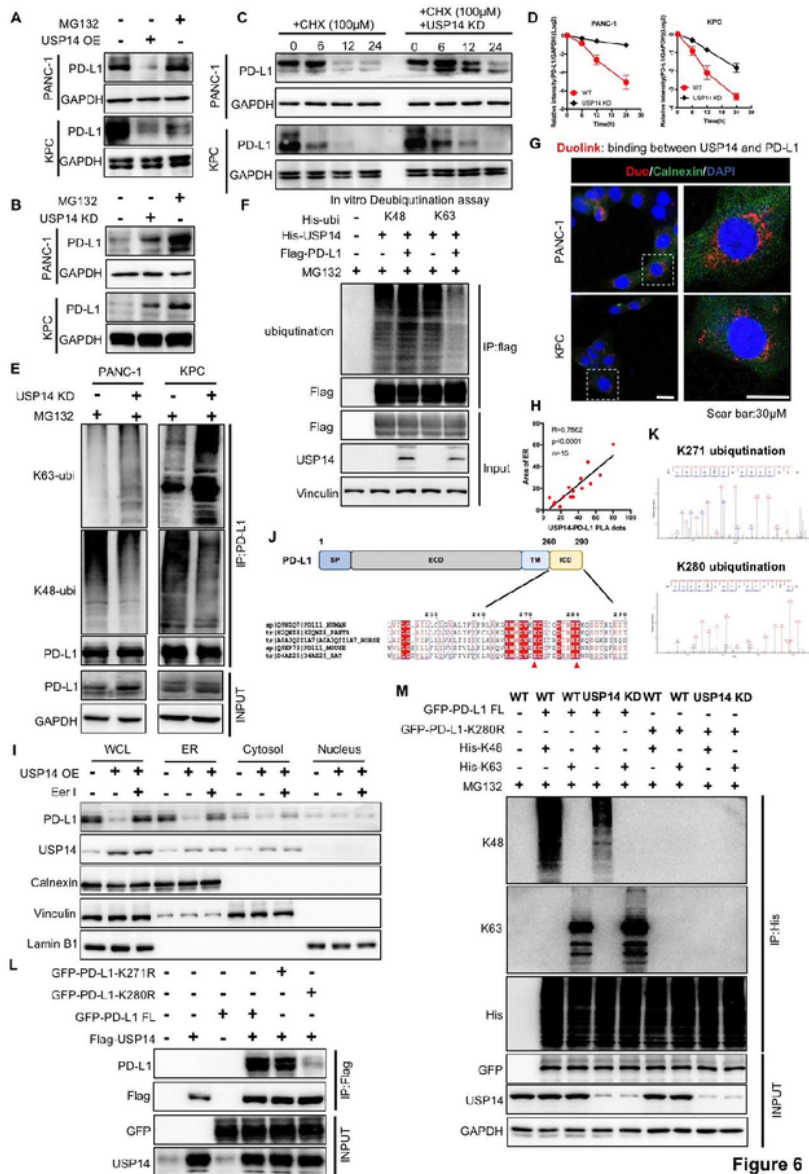


Figure 6

Figure 6

USP14 destabilizes PD-L1 and specifically removes the K63-linked poly-ubiquitination of PD-L1 at the K280 residue.

(A and B) Immunoblot analysis of PD-L1 expression in tumor cells with USP14 overexpression or knockdown after treatment with MG132.

- (C and D) Stability analysis of PD-L1 in tumor cells with USP14 knockdown following treatment with cycloheximide (CHX).
- (E) Ubiquitination assay of PD-L1 in tumor cells with an USP14 knockdown after treatment with MG132.
- (F) In vitro deubiquitination assays of recombinant USP14 proteins and enriched K48-linked or K63-linked ubiquitinated PD-L1 from cell extracts. The mixture was incubated at 30°C for 4 h and subsequently analyzed by immunoblotting.
- (G and H) Representative images and statistical results of the tumor cells were subjected to a Duolink assay combined with immunofluorescence staining using markers for ER (Calnexin) and nuclei (DAPI).
- (I) Immunoblot analysis of PD-L1 and USP14 in different fractions, using antibodies against PD-L1 and USP14, the ER protein calnexin, cytosolic α -Tubulin, as well as the nuclear protein, Lamin B1.
- (J) Schematic diagram of the USP14-binding motif in amino acid sequences surrounding the potential binding sites of PD-L1 that were aligned in evolutionarily divergent species.
- (K) The ubiquitination site on PD-L1 as identified by mass spectrometry.
- (L) Immunoblot analysis of PD-L1 expression in flag-USP14 and GFP-PD-L1 FL or GFP-PD-L1-K271R or GFP-PD-L1-K280R-transfected HEK293T cells.
- (M) Ubiquitination assay of PD-L1 in USP14 WT and USP14 knockdown HEK293T cells transfected with GFP-PD-L1 FL or the GFP-PD-L1-K280R were subjected to His pull-down and SDS-PAGE analyses.

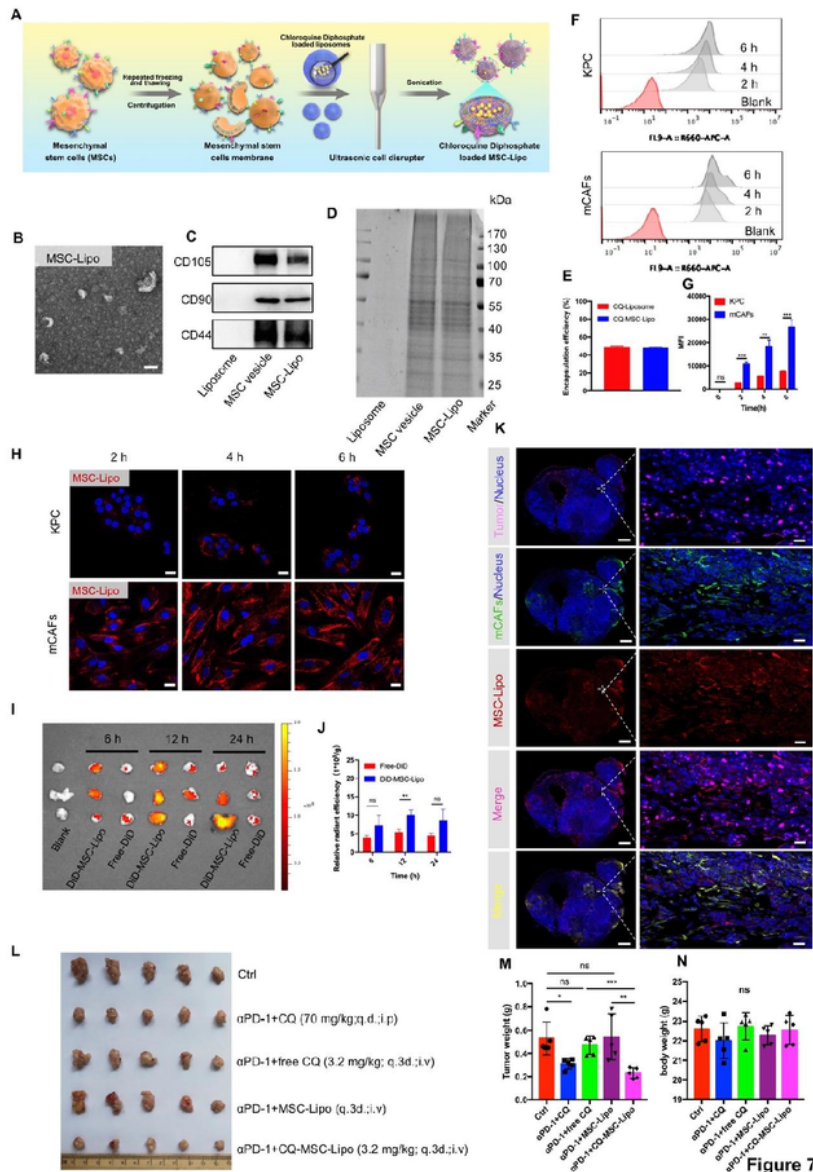


Figure 7

Targeting CAF autophagy renders primary PDAC tumors eradicable by immunotherapy via engineering stem cell-derived biomimetic vesicles

(A) The preparation, characterization, and targeting of the therapeutic application of MSC-Lipo.

(B) Transmission electron microscopic image of MSC-Lipo. Scale bar: 100 nm.

(C) Immunoblot analysis of liposomes, MSC vesicles, and MSC-Lipo for specific surface markers (CD105, CD90, and CD44).

(D) SDS-PAGE analysis of the protein contents of liposomes, MSC vesicles, and MSC-Lipo. (E) Encapsulation efficiency of CQ-loaded liposomes and MSC-Lipo (n=3).

(F) Flow cytometry analysis of MSC-Lipo uptake by KPC and mCAFs at 2 h, 4 h and 6 h and 12 h.

(G) Quantification of fluorescence intensity (n = 3).

(H) KPC and CAFs uptake MSC-Lipo at 2 h, 4 h and 6 h as captured by a confocal laser scanning microscope (red: DiD and blue: DAPI). Scale bar: 20 μ m.

(I) The distribution and (J) relative radiant efficiency of free-DiD and DiD-MSCLipo in tumors at 6 h, 12 h and 24 h after intravenous injection (n = 3).

(K) Colocalization of MSC-Lipo with KPC and CAFs in the tumor sections at 12 h after an intravenous injection (red: DiD, green: CD326, pink: α -SMA and blue: DAPI). Scale bar: 2 mm for the original images and 100 μ m for the magnified images.

(L) Photography of tumors at the ending of treatment (n = 5). Tumor weight (M) and body weight (N) at the end of treatment (n = 5).

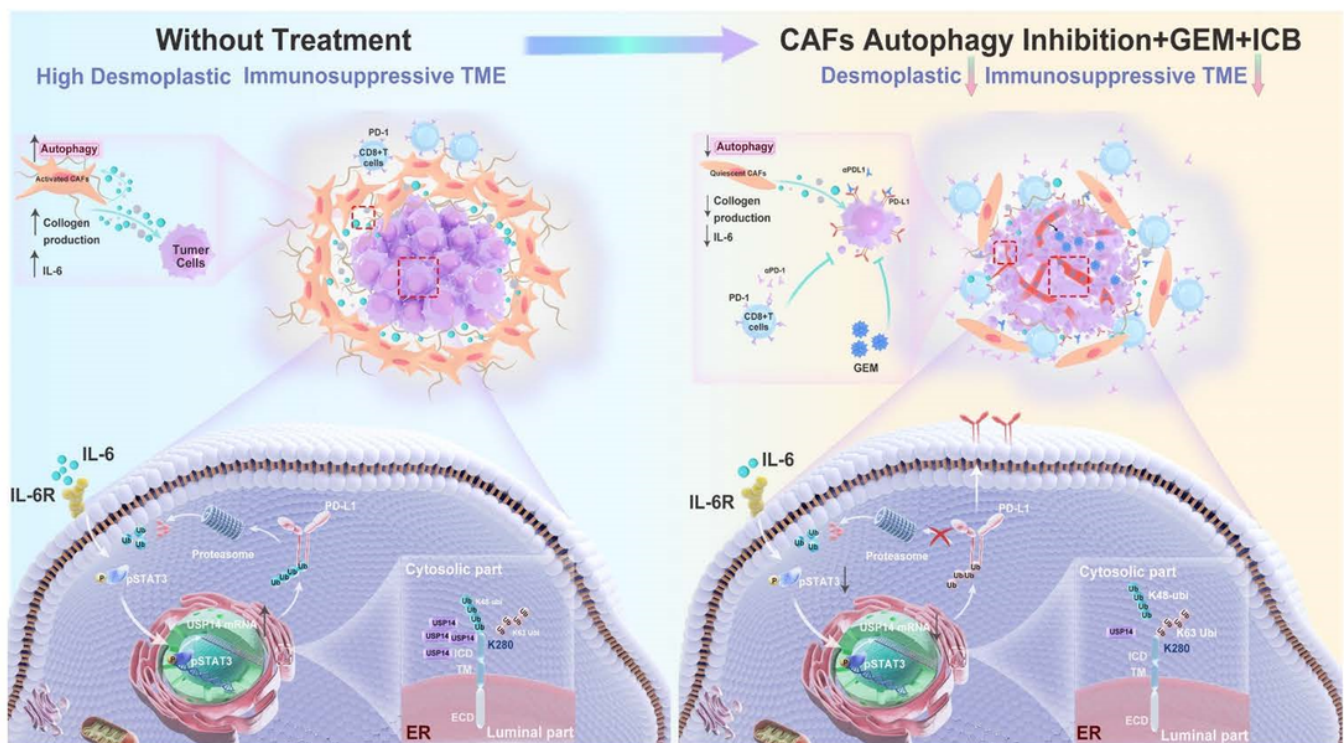


Figure 8

Legend not included with this version

Supplementary Files

This is a list of supplementary files associated with this preprint. Click to download.

- [FigureS121.pdf](#)
- [SUPPLEMENTALFIGURELEGENDS.docx](#)
- [SupplementalMaterialsandMethods.docx](#)
- [SupplementaryTable1.docx](#)